High Tolerance to Iron Contamination in Lead Halide Perovskite Solar Cells

Jeremy R. Poindexter,[*,†] Robert L. Z. Hoye,[†,⊥] Lea Nienhaus,[†] Rachel C. Kurchin,[†]
Ashley E. Morishige,[†] Erin E. Looney,[†] Anna Osherov,[†] Juan-Pablo Correa-Baena,[†] Barry Lai,[‡]
Vladimir Bulović,[†] Vladan Stevanović,[∥,§] Moungi G. Bawendi,[†] and Tonio Buonassisi[*,†]

[†]Massachusetts Institute of Technology, 77 Massachusetts Avenue, Cambridge, Massachusetts 02139, United States
[‡]Advanced Photon Source, Argonne National Laboratory, 9700 Cass Avenue, Lemont, Illinois 60439, United States
[∥]Colorado School of Mines, 1500 Illinois Street, Golden, Colorado 80401, United States
[§]National Renewable Energy Laboratory, 15013 Denver West Parkway, Golden, Colorado 80401, United States

S *Supporting Information*

ABSTRACT: The relationship between charge-carrier lifetime and the tolerance of lead halide perovskite (LHP) solar cells to intrinsic point defects has drawn much attention by helping to explain rapid improvements in device efficiencies. However, little is known about how charge-carrier lifetime and solar cell performance in LHPs are affected by extrinsic defects (*i.e.*, impurities), including those that are common in manufacturing environments and known to introduce deep levels in other semiconductors. Here, we evaluate the tolerance of LHP solar cells to iron introduced *via* intentional contamination of the feedstock and examine the root causes of the resulting efficiency losses. We find that comparable efficiency losses occur in LHPs at feedstock iron concentrations approximately 100 times higher than those in p-type silicon devices. Photoluminescence measurements correlate iron concentration with nonradiative recombination, which we attribute to the presence of deep-level iron interstitials, as calculated from first-principles, as well as iron-rich particles detected by synchrotron-based X-ray fluorescence microscopy. At moderate contamination levels, we witness prominent recovery of device efficiencies to near-baseline values after biasing at 1.4 V for 60 s in the dark. We theorize that this temporary effect arises from improved charge-carrier collection enhanced by electric fields strengthened from ion migration toward interfaces. Our results demonstrate that extrinsic defect tolerance contributes to high efficiencies in LHP solar cells, which inspires further investigation into potential large-scale manufacturing cost savings as well as the degree of overlap between intrinsic and extrinsic defect tolerance in LHPs and "perovskite-inspired" lead-free stable alternatives.

KEYWORDS: photovoltaics, methylammonium lead iodide, extrinsic defects, impurities, photoluminescence, hysteresis, recombination
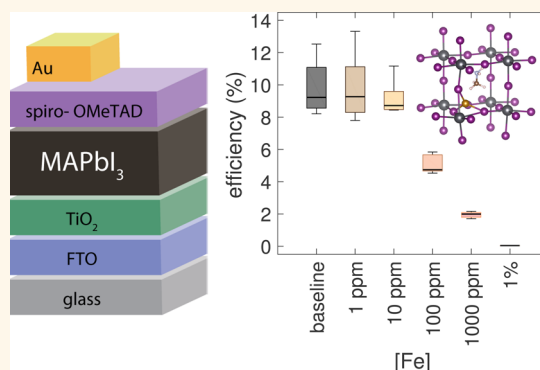
The development of lead halide perovskite (LHP) solar cells, which now exceed 20% efficiency,[1–3] has invigorated the photovoltaics (PVs) community by eclipsing the traditionally slow rate of progress in PV materials and device engineering, improving prospects for thin-film PV technologies to reach global scale and mitigate climate change.[4] Both the rapid rate of improvement since early efforts[5–7] and more recent high performance in LHPs have been enabled by long charge-carrier lifetimes exceeding 100 ns.[8–10] Theoretical studies suggest that intrinsic point defects in LHPs contribute relatively little to Shockley–Read–Hall recombination due to their tendency to demonstrate (1) shallow levels within the band gap and/or (2) high formation enthalpies that reduce their bulk concentration, both of which contribute to long lifetimes and hence the material's "defect tolerance".[11–13] However, most attention has focused on the effect of intrinsic rather than extrinsic point defects (*i.e.*, impurities), the latter of which are known to significantly degrade performance at concentrations at or below 1 ppm in some semiconductors— most notably in silicon and III–V compounds.[14–18] Currently, device performance limitations due to impurity contamination remain an unknown and potentially challenging impediment for the pursuit of further efficiency gains and scale-up of LHPs and related lead-free stable alternatives. Such impurity incorporation may unintentionally occur during solution synthesis, which is frequently used to fabricate LHPs,[5,19] as the polar solvents often used to form precursor solutions can readily
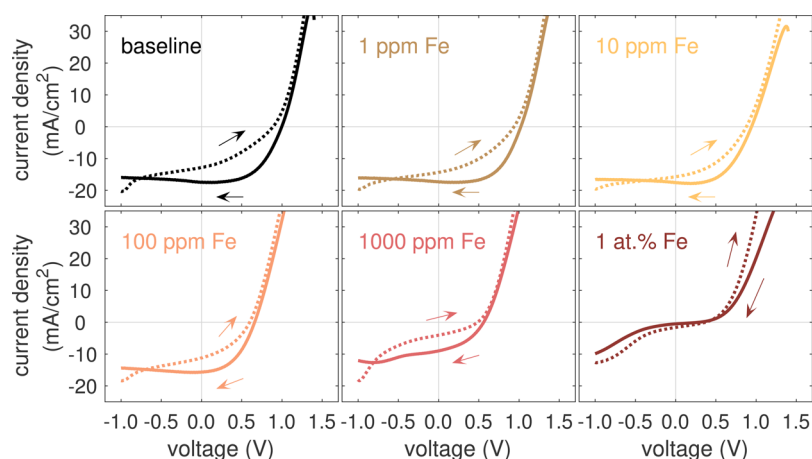
Figure 1. $J-V$ sweeps taken with a scan speed of 0.1 V/s in the reverse (solid lines) and forward (dotted lines) directions under 1 sun illumination and a N_2 ambient at five intentional feedstock iron contamination levels plus a baseline, which was not intentionally contaminated. For each sample, the plot shown is the device closest to the median efficiency of 7−8 devices on each sample. For $J-V$ sweeps measured after prebiasing, see Figure S1, Supporting Information.

dissolve many impurity-containing substances unknown to be present in feedstocks.

Some previous work has explored how precursor purity may affect device performance,[20] as well as how certain extrinsic species may affect electronic properties in LHPs via doping,[21,22] which has been shown to increase device performance.[23−25] Calculations by Shi et al.[26] suggest that alkali cations, oxygen, and halogens form shallow levels in methylammonium lead iodide (MAPbI$_3$); however, theoretical studies of the effect of 3d transition metals, the most detrimental contaminants in silicon and III−V compounds, are lacking. Experimentally, Klug et al.[27] found that device efficiencies in MAPbI$_3$ could be maintained among high levels (exceeding 1 at.%) of certain transition metals in the precursor solutions used, suggesting some degree of extrinsic defect tolerance. Iron, the most detrimental transition metal in that study, caused efficiency losses of ∼70% at an Fe:Pb ratio of 1:63 (equal to a feedstock iron concentration of approximately 1300 ppm). These results warrant further investigation of the relationship between impurity concentration and (1) nonradiative recombination as well as (2) device efficiency, so that contamination thresholds (including those more representative of unintentional contamination) can be better compared between materials.

Here, we fabricate and characterize LHP solar cells intentionally contaminated with iron at five feedstock impurity concentrations ranging from 1 to 10 000 ppm (i.e., 1 at.%) alongside a baseline sample, which was not intentionally contaminated. We choose iron due to its prevalence in PV manufacturing settings[28,29] (e.g., in stainless steel tubing and machinery) and its known detrimental effect in silicon,[30−32] III−V compounds,[15,16,18] and other PV materials such as copper zinc tin sulfide−selenide,[33] forming deep levels within the band gap and often having large carrier capture cross sections. Our results suggest that performance in LHP solar cells begins to decrease significantly at iron concentrations between 10 and 100 ppm, demonstrating tolerance to iron at feedstock concentrations up to 100 times higher than that in representative p-type silicon solar cells.[30,34] Nonetheless, we observe that iron concentration correlates with increased nonradiative recombination, and calculations using density functional theory suggest that iron interstitials form deep levels within the band gap. Device hysteresis and the effect of

prebiasing on device performance highlight the role of electric fields in preventing electron−hole recombination that may occur both throughout the bulk and at coarsely dispersed iron-rich areas that form in the most highly contaminated films. We discuss the implications of these findings to manufacturing costs and the development of "perovskite-inspired" lead-free stable alternatives.

RESULTS

We fabricated LHP films and devices by slightly modifying a standard recipe[6] that combines methylammonium iodide with lead(II) chloride in a 3:1 molar ratio to form MAPbI$_3$ with trace amounts of Cl. Solar cells were fabricated in a glass/FTO/TiO$_2$/MAPbI$_3$/spiro-OMeTAD/Au architecture; see Supporting Information for further fabrication details. Iron(II) iodide (FeI$_2$) served as our contamination source and readily dissolved in the N,N-dimethylformamide solvent. Based on the standard reduction potentials of Fe^{3+}|Fe^{2+}, Fe^{2+}|Fe, and I$_2$|I$^-$, we expect FeI$_2$ to fully dissolve and remain stable as separate Fe^{2+} and I$^-$ ions. We note that throughout this article we refer to the iron concentration introduced to the feedstock solution. To assess the impact of iron incorporation on photovoltaic performance, we measured current-density vs voltage ($J-V$), shown in Figure 1. Solar cell parameters from all 7−8 devices (each with an area of 0.25 cm^2) on each sample, taken in the reverse direction with and without a presweep voltage bias of 1.4 V in the dark for 60 s, are summarized in Figure 2. As the iron concentration increases from the baseline sample to 10 ppm, the open-circuit voltage (V_{OC}) and short-circuit current density (J_{SC}) without any prebias change only slightly. Above 10 ppm, however, the devices suffer considerable losses in both V_{OC} and J_{SC} and thus device efficiency (Figures 1 and 2). Additionally, "rollover" in the $J-V$ curves begins to manifest at 1000 ppm (Figure 1), contributing to J_{SC} losses. The monotonically decreasing trend in V_{OC} without any prebias is consistent with an expected increase in recombination. Due to prebias effects and the use of a relatively slow scan rate of 0.1 V/s, which corresponds to an effective 4−10 s prebias above V_{OC}, the absolute values for the solar cell parameters may change slightly for different scan rates.

To correlate $J-V$ performance with charge-carrier lifetime, we measured time-resolved photoluminescence (TRPL) on
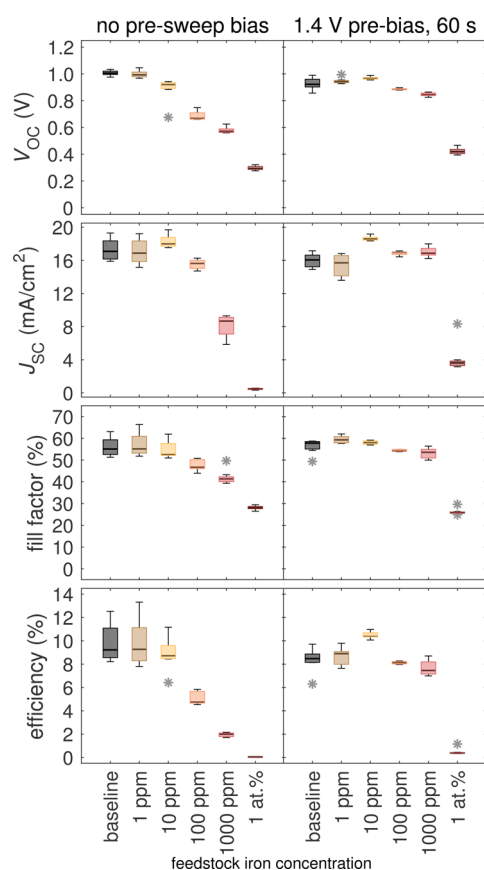
Figure 2. Boxplot summary of $J-V$ parameters for sweeps taken in the reverse direction with (right column) and without (left column) a 1.4 V presweep bias taken in the dark for 60 s. Box upper and lower bounds represent 75 and 25% percentile marks, respectively. Whiskers indicate data extrema up to 2.7 standard deviations away from mean. Asterisks represent outliers (more than 2.7 standard deviations away from mean). For corresponding summary of sweeps taken in forward bias, see Figure S2, Supporting Information.

glass/TiO$_2$/MAPbI$_3$ films under ambient air using time-correlated single-photon counting. The spiro-OMeTAD layer was omitted to decrease the effect of photoluminescence (PL) quenching caused by the selective extraction of holes at the MAPbI$_3$/spiro-OMeTAD interface,[8] and the films were deposited on TiO$_2$ to ensure that the film morphology (shown in Figure S3; see Supporting Information) remained similar to that of the full devices. Since the 500 nm thickness of our MAPbI$_3$ films exceeds the absorption depth (approximately 150 nm, for 532 nm wavelength excitation) by over a factor of 3, we do not expect significant PL quenching from the TiO$_2$/MAPbI$_3$ interface. The TRPL decay curves, shown in Figure 3a, indicate generally decreasing PL decay times with increasing iron concentration, although differing behavior occurs between the 10 and 100 ppm films, the former of which has a faster initial decay but a longer tail. Estimated lifetimes obtained from monoexponential fits to the data are listed in Table 1. While

Table 1. Incorporated Iron Concentration and Fitted Charge-Carrier Lifetimes for Iron-Contaminated Films

sample	incorporated iron concentration (ppm)	monoexponential fit time constant (ns)
baseline		325
1 ppm		314
10 ppm		148
100 ppm		138
1000 ppm	1076 ± 158	32
1 at.%	3332 ± 171	30

these specific values may not accurately represent lifetimes in devices under operation, in part due to the non-monoexponential behavior at early PL decay times (see Figure 3a, inset), the trend with iron concentration more directly links losses in device efficiency to nonradiative recombination.

To evaluate how much iron incorporates into the films during growth, impurity concentration measurements were performed by dissolving MAPbI$_3$ films in dilute nitric acid and analyzing the contents with inductively coupled plasma optical emission spectroscopy (ICP-OES). Calculated incorporated
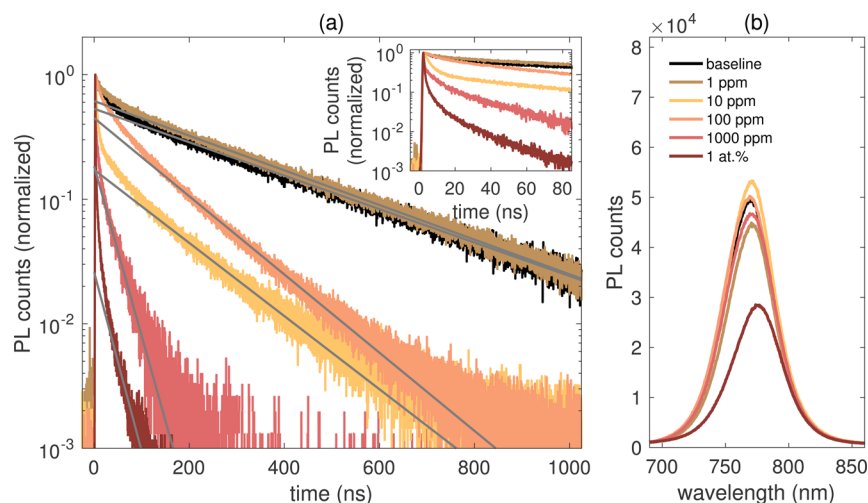

Figure 3. (a) Time-resolved photoluminescence on sister samples (glass/TiO$_2$/MAPbI$_3$) fabricated under the same conditions as devices but without FTO or absorber overlayers, collected using 532 nm excitation at 0.8 nJ/cm^2 fluence at 500 kHz with 650 nm long pass, 800 nm short pass, and 532 nm notch filters, respectively. Inset shows early time scale PL dynamics. Gray lines indicate monoexponential fits to the data; see Table 1. (b) Spectral photoluminescence measurements collected with a 532 nm excitation and a 0.2 s exposure time.
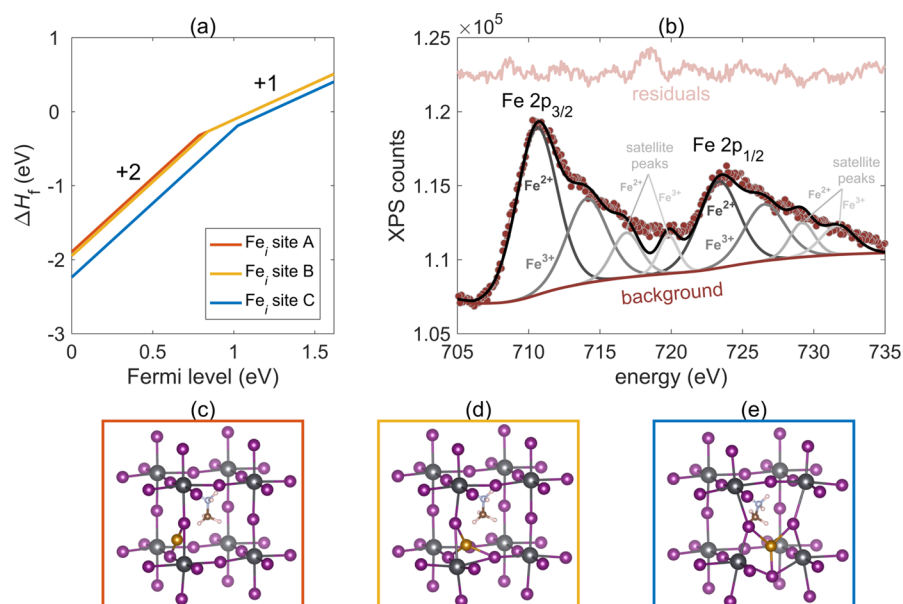
Figure 4. (a) Defect energy level diagram calculated from density functional theory for three symmetry-inequivalent Fe_i sites in $MAPbI_3$. (b) X-ray photoelectron spectroscopy measurements of Fe 2p peaks for a feedstock iron concentration of 1 at.% showing experimental data (maroon circles) and fit to the data (black line) broken down into individual peaks (gray lines). (c−e) $MAPbI_3$ crystal structure for Fe_i (golden spheres) incorporated at sites A, B, and C, respectively, alongside lattice sites for Pb (black), I (purple), C (brown), N (light gray), and H (pink).
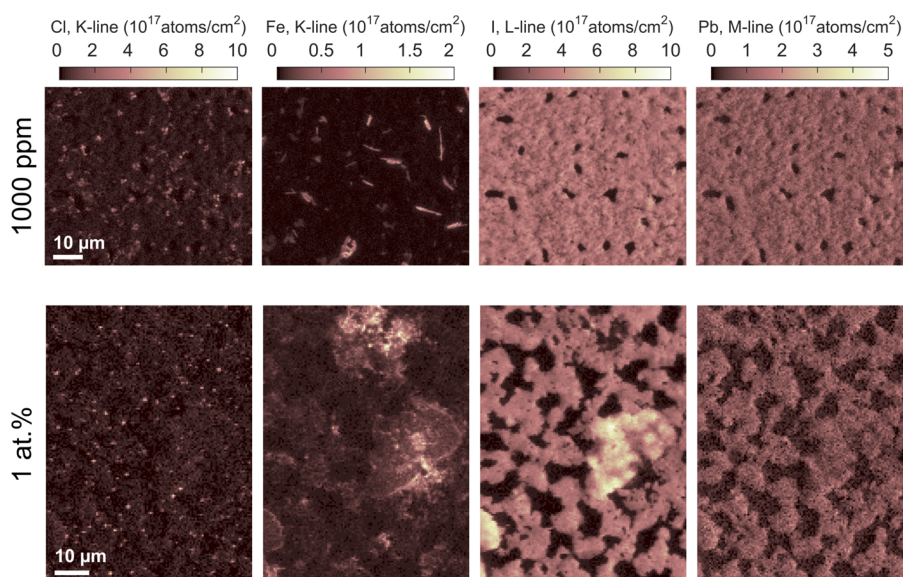

Figure 5. Synchrotron-based X-ray fluorescence microscopy maps of glass/TiO_2/$MAPbI_3$/Au films at 1000 ppm (top row) and 1 at.% (bottom row) feedstock iron contamination levels; 40 nm of Au was deposited onto the films to dissipate charging from the beam.

iron concentrations, also listed in Table 1, show that for our fabrication conditions, the incorporation of iron saturates near 3300 ppm, or 0.3 at.%. Precise concentrations below 1000 ppm were not able to be determined within a tolerance of 100 ppm due to uncertainty; see Experimental Methods for details.

Figure 3b shows that a decrease in the spectrally resolved PL intensity occurs at 1 at.%. We note that the spectral PL measurements were performed at the same wavelength but with a different repetition rate and output power, compared to the TRPL measurements; see Experimental Methods. The slight red shift in the PL spectrum of the 1 at.% film is characteristic of a decrease in the total charge-carrier population, which causes states farther from the band edges to remain empty and

thus lowers the peak energy of the PL without significantly altering the shape of the PL profile itself.

Our results thus far demonstrate an inverse correlation between nonradiative recombination and J−V performance. However, it remains unclear what specific defect(s) causes recombination. Possibilities include interstitial iron, iron substituting on lead (or other) sites, defect complexes, iron-decorated dislocations or grain boundaries, and agglomerates of precipitated iron or iron-containing phases (e.g., FeI_2, $FeCl_2$). To begin exploring which defects may be both present and detrimental to device performance, we investigate a few possibilities using first-principles defect calculations and X-ray spectroscopy techniques.

Formation-energy calculations for iron point defects in MAPbI$_3$ using density functional theory indicate that iron interstitials (Fe$_i$), shown in Figure 4a, are by far the most likely to form, as calculated formation energies for substitutional iron on the lead (Fe$_{Pb}$), iodine (Fe$_I$), and methylammonium (Fe$_{MAI}$) sites all exceeded 10 eV (at the valence band maximum). Due to slight distortions in the tetragonal structure[35] of room-temperature MAPbI$_3$, there are three symmetry-inequivalent Fe$_i$ sites, leading to multiple defect energy levels occurring at the +2/+1 transition. All three levels, however, lie more than 0.5 eV from either band edge and thus can be considered "deep".[36] Fitted X-ray photoelectron spectroscopy (XPS) measurements on the 1 at.% film, shown in Figure 4b, suggest iron in both +2 and +3 charge states may be present while metallic iron (whose binding energy lies near 707 eV) is absent, as indicated by the position of the main Fe 2p$_{3/2}$ peak near 710 eV.[37,38] However, we do observe local agglomeration of iron at high concentrations, as shown from synchrotron-based X-ray fluorescence microscopy (μ-XRF) maps in Figure 5. In the 1000 ppm film, these iron-rich agglomerates appear to be needlelike in shape, whereas in the 1 at.% film, iron is more broadly distributed. No metallic iron was detected via XPS, which suggests these iron-rich agglomerates may comprise Fe^{2+}-containing compounds such as FeI$_2$ and/or FeCl$_2$, although further studies (e.g., X-ray absorption) are needed to verify this. The micron-scale variations in lead and iodine content, particularly evident in the 1 at.% film, are due to nonuniform film morphology (see Figure S3, Supporting Information).

DISCUSSION

Overall, MAPbI$_3$ solar cells contaminated with iron suffer a 50% relative drop in efficiency around 100 ppm, compared to around 1 ppm for representative p-type silicon devices.[30,34] Whereas direct comparisons with silicon-based devices depend on their device architecture, processing, operating injection level, and the specific defect considered (e.g., iron interstitials vs iron–boron pairs), only under particular conditions (i.e., certain architectures in high injection) can p-type silicon devices retain over 50% of their baseline efficiency when contaminated with 100 ppm of iron in the feedstock. Thus, in comparison to p-type silicon, MAPbI$_3$ seems to tolerate up to 100 times more iron despite the presence of deep levels within the band gap due to iron interstitials. Moreover, considering that we compare feedstock iron concentrations here, our comparison likely underestimates the tolerance of MAPbI$_3$ to iron, as in silicon solar cell fabrication, much of the iron initially present in the bulk is removed by gettering processes.[39,40] It is worth noting that n-type silicon solar cells are far more tolerant to interstitial iron as its capture cross section for holes in silicon is over 100 times smaller than that for electrons.[41,42]

It is particularly remarkable that charge-carrier lifetimes in MAPbI$_3$ dropped only an order of magnitude or so while feedstock iron concentration increased by 4 orders of magnitude from 1 to 10 000 ppm (1 at.%). From Shockley–Read–Hall recombination statistics, we expect a linear correlation between lifetime and defect concentration;[43,44] thus, the observed trend suggests that feedstock iron concentrations up to 100 ppm do not limit lifetime in MAPbI$_3$ as they do in p-type silicon,[28] and/or that much of the iron present acts differently than a Shockley–Read–Hall-type defect (e.g., is located at the surfaces of precipitates). We note that this specific result might be influenced by the specific

solution chemistry used, which could affect the size and shape of iron-rich particles seen in Figure 5, which in turn may affect film morphology. Iron incorporated via other methods (e.g., a thin sheet of metallic Fe deposited on top of TiO$_2$ prior to spin-coating) might affect nucleation differently. Hence, the contamination technique may result in different geometries of iron-rich particles and thus different recombination behavior in highly contaminated samples where such particles are observed.

Considering that the 1 at.% device maintained a relatively long lifetime in the tens of nanoseconds, its 0.04% device efficiency seems disproportionately low, dominated by a very low J_{SC} (0.51 mA/cm^2). This may be due decreases in charge-carrier mobility due to impurity scattering, which is expected to increase at higher iron concentrations. It is also possible that the observed local film inhomogeneities (see Figure S3, Supporting Information) affect carrier transport pathways, or that interface band offsets affect charge-carrier collection (and to some extent, V_{OC}) at the interface.[45] In particular, voids could affect the amount of shunting and light absorption that occurs in the devices, though we see little evidence of the former effect in the J–V response in our devices. Moreover, neither effect is likely to fully explain the sharp decrease in J_{SC} seen at high contamination levels. Other variations in the film, such as excess PbI$_2$, as evident via X-ray diffraction (XRD) (see Figure S4, Supporting Information), might affect overall recombination behavior. Our XRD analysis did not reveal the presence of any binary or ternary impurities containing combinations of (Ti, Fe, Pb) and (O, Cl, I), though such species may be present in small amounts undetectable by XRD.

Other factors may also affect the recombination activity of iron. Whereas bulk XPS measurements suggest a mix of Fe^{2+} and Fe^{3+}, the lack of a +3/+2 transition within the band gap as calculated by DFT suggests that Fe$_i^{3+}$ is not recombination active as a point defect. Fe$_i^{2+}$ may readily form in high concentrations (limited by the initial feedstock iron concentration) due to its low formation energy, although we stress that calculating interstitial concentrations from formation energies may be misguided because DFT calculations capture thermodynamic behavior, whereas our films are synthesized at low temperatures (100 °C) unlikely to satisfy thermodynamic equilibrium. The remarkably high formation energies (above 10 eV) of all three possible iron substitutional defects (Fe$_{Pb}$, Fe$_I$, and Fe$_{MAI}$) may help limit the solubility of point defect iron in MAPbI$_3$ to lower levels, causing iron to instead agglomerate into larger particles in the presence of supersaturation, as suggested by μ-XRF. This effect, if present, may reduce overall recombination, similar to how precipitates in p-type silicon are known to be less detrimental compared to that same amount of iron distributed as point defects.[46–48] Furthermore, despite having a deep defect energy level, the capture cross section for iron, if small enough, may allow it to avoid being particularly recombination active, as has been seen in GaAs, where iron incorporates substitutionally.[15] The high static dielectric constant of MAPbI$_3$ of 60 or larger[49,50] may play a role in screening the charge of Fe$_i^{2+}$ and contributing to a low capture cross section. In this way, a high dielectric constant may contribute to both extrinsic and intrinsic defect tolerance in LHPs.

Despite uncertainties about iron's specific chemical and structural characteristics in MAPbI$_3$, we see evidence that it generates trap states within the bulk through two effects on J–V: (1) the improvement in performance after prebiasing and (2) the correlation of "rollover" with iron concentration. First,

we observe that devices with higher contamination levels (between 10 and 10 000 ppm) show recovery in both J_{SC} and V_{OC} after applying a presweep voltage bias at 1.4 V for 60 s in the dark and sweeping in the reverse direction. In some cases, J_{SC} values recover completely or even exceed that of the baseline. These performance improvements are temporary, however, and the forward-direction $J-V$ response remains similar regardless of any prebias (see Figure S1 and Figure S2, Supporting Information). All of these observations are consistent with bias effects reported previously,[51,52] which suggest that charged mobile ions migrate toward interfaces, where they generate space charge and thus screen the built-in voltage within the bulk. Then, once a bias voltage is applied, these ions redistribute away from interfaces, reducing screening and resulting in enhanced charge-carrier collection. That this effect correlates with iron concentration suggests that iron limits charge-carrier transport within the film.

Second, we posit that the "S-shape" or "rollover" that emerges in the $J-V$ response above 100 ppm may be related to the presence of iron within the bulk. MAPbI$_3$ device modeling performed by van Reenen et al. (see Supporting Information in ref 53) suggests that trap states within the bulk—not only those at interfaces—can cause hysteresis and that observed "rollover" can be related to hysteresis itself. The trend in hysteresis in our devices is consistent with this interpretation. Furthermore, we also observe this trend in devices fabricated using the "inverted" perovskite device architecture;[54] see Supporting Information for device fabrication details. Figures S6 and S7 (see Supporting Information) show that for this alternative architecture, $J-V$ hysteresis begins to manifest at 100 ppm, as does the improvement in device performance due to the presweep bias. This similarity in trends of hysteresis and the effect of presweep bias within two distinct LHP architectures suggests that bulk charge-carrier transport effects may dominate over interface characteristics, although it is possible a correlation between interface band offset and iron concentration could still contribute.

The observation of high tolerance of LHPs to iron inspires several questions that may affect future efforts to scale-up LHPs and related "perovskite-inspired" lead-free stable alternatives. Increased tolerance to iron may translate to manufacturing cost savings by enabling the use of lower-purity precursors, manufacturing environments (e.g., cleanrooms) with less stringent particle-count requirements, and wider materials selection for processing equipment, for example. These savings will depend on baseline manufacturing processes but could be significant, especially considering the high costs of silicon precursor purification (to at least 99.9999%), which comprise approximately one-third of the polysilicon-to-module factory capital costs.[55]

Additionally, the particular characteristics of iron in LHPs—namely, the ability to incorporate high concentrations within the bulk despite deep levels within the band gap—provoke further inquiry into whether intrinsic and extrinsic defect tolerance both arise from similar mechanisms. For example, high dielectric constants are expected to reduce the effective capture cross section of any charged point defect, whether intrinsic or extrinsic, whereas the underlying principles that are most important in determining defect energy levels (e.g., orbital alignment of atoms, antibonding character, local bonding environment) may differ for intrinsic vs extrinsic point defects. In light of emerging efforts to design and develop lead-free and stable alternatives to LHPs[56-61] while retaining their defect-tolerance properties, understanding how materials structure and chemistry affect defect tolerance may be critical to properly assess the risk of impurity incorporation in slowing—or even limiting—improvements in device efficiencies.

CONCLUSIONS

In summary, we find that MAPbI$_3$ devices can tolerate approximately 100 times higher feedstock iron concentrations compared to representative p-type silicon devices before comparable efficiency losses occur. $J-V$ performance suggests that iron contributes a significant number of trap states, as performance losses can be temporarily recovered by applying a presweep dark voltage bias that likely enhances electric-field-assisted charge-carrier collection. Regardless, charge-carrier lifetimes remain in the tens of nanoseconds even when bulk iron concentration exceeds 3000 ppm, demonstrating remarkable tolerance to the presence of iron, especially given that iron interstitials form deep levels. This experimentally demonstrated tolerance of MAPbI$_3$ to iron helps explain high PV performance in LHPs despite the use of synthesis techniques where impurities are likely present. These findings provide the initial groundwork for evaluating the effect of feedstock purity on large-scale LHP solar cell manufacturing costs, and the framework herein points toward deeper understanding of the mechanisms that affect both extrinsic and intrinsic defect tolerance that could inform efforts to develop "perovskite-inspired" lead-free stable photovoltaic materials.

EXPERIMENTAL METHODS

Solar cell characterization of glass/FTO/TiO$_2$/MAPbI$_3$/spiro-OMe-TAD/Au devices was performed in a nitrogen-filled glovebox under 1 sun conditions using a solar simulator (Newport Oriel, model 69907) and a semiconductor device analyzer (Agilent Technologies, model B1500A). Scans were performed from +1.4 V to −1 V, then immediately from −1 to +1.4 V at a scan speed of 0.1 V/s in both directions. The device area of 0.25 cm^2 was determined by the area of the Au contact pad; apertures were not used because edge effects were found to be negligible. For scans taken after the presweep bias, reverse and forward scans were performed under these same conditions after a 1.4 V was applied in the dark for 60 s immediately beforehand.

Time-resolved photoluminescence measurements were collected using a time-correlated single-photon counting setup that used a 532 nm wavelength picosecond laser (PicoQuant, LDH-P-FA-530B) pulsed at 500 kHz. The power for all measurements was 102 nW, which along with a beam spot size of 180 μm^2 corresponds to a photon fluence of 0.8 nJ/(cm^2·pulse), or 2.2×10^9 photons/(cm^2·pulse). For an absorption coefficient of 6.5×10^4 cm^{-1} and lifetime of 100 ns, this corresponds to an injection level of ~0.1 suns. PL emission was captured using parabolic mirrors and focused on a single-photon avalanche photodiode (Micro Photon Devices, \$PD-100-C0C). Photon arrival times were detected using a time synchronizer (PicoQuant, PicoHarp 300).

Spectral photoluminescence measurements were collected using a 532 nm laser (CrystaLaser, model QL262-030) pulsed at 1.2 kHz with an average output power of 50 mW, a 300 mm focal length triple grating monochromator (Princeton Instruments, Acton SP2300) and a CCD for detection (Princeton Instruments, model 7516-0002). Exposure time was 0.2 s. The error in total PL counts is approximately ±15% due to time-dependent emission behavior and slight variations (±10 s) in the time between beam turn-on and data collection. No significant shift in PL energy was seen after 130 s of illumination.

Iron impurity content measurements were performed using ICP-OES (Agilent Technologies, 5100 ICP-OES) by dissolving films in a dilute (2% v/v, JT Baker, 99.9999%) nitric acid matrix and analyzing the elemental spectra using both horizontal and axial views. High-density polypropylene containers were soaked in the nitric acid matrix

for over 48 h and then rinsed with the same solution to leech out and remove any container contaminants. To obtain quantitative iron incorporation data, standard solutions for both iron (Inorganic Ventures, 10 ppm) and lead (Inorganic Ventures, 100 ppm) were prepared with 0.001, 0.01, 0.05, 0.1, 0.5, 1, 5, and 10 μg/mL of iron and 10, 50, and 100 μg/mL of lead in solution, respectively. The raw signal counts were collected and averaged at five distinct spectral lines for each element and then compared between these standards and the samples to determine total iron content. Due to cross-interference between iron and lead in the solutions, uncertainty for the baseline, 1, 10, and 100 ppm samples was higher than 100 ppm; thus, the numbers are not reported in Table 1.

Density functional theory calculations were performed with space group $P4mm$ using the VASP code[62] and the standard Perdew–Burke–Ernzerhof functional.[63] All point defect calculations were performed utilizing the supercell approach as described previously[64,65] and implemented in the automated framework of Goyal et al.[66] A 3 × 3 × 3 supercell was, with each supercell containing 324 atoms and periodic images separated by at least 19.5 Å. Calculations for supercells were performed at a single k-point, with the host lattice computed on a 6 × 6 × 6 Monkhorst–Pack grid,[67] all using a plane-wave cutoff of 340 eV. Finite size corrections including image charge correction for charged defects, band alignment, and band filling corrections have been employed, and chemical potentials from the fitted elemental reference energies were used.[68] Point defects considered in this study included iron substituting on the lead, methylammonium, and iodine sites as well as iron sitting at three symmetry-inequivalent interstitial sites (see Figure 4), which were identified using the framework of Goyal et al.[66] Only the interstitial defects were found to be low enough in energy to be relevant and were computed in charge states $q = -2, -1, 0, +1, +2, +3$, and $+4$.

X-ray photoelectron spectroscopy measurements were collected using a Thermo Scientific K-Alpha X-ray spectrophotometer. Peaks were fitted and analyzed using Thermo Avantage software; Gaussian mixture was used. Baseline was calculated using Shirley's method, and the data were corrected assuming atmosphere carbon contamination at 285 eV. No beam-induced degradation or sample charging was apparent, as evidenced by the persistence of Pb and N peaks at the sample surface.

Synchrotron-based X-ray fluorescence microscopy was performed at beamline 2-ID-D at the Advanced Photon Source, Argonne National Laboratory,[69] at an excitation energy of 9 keV with a 200 nm spot size, step sizes of 500 nm (1000 ppm film) and 220 nm (1 at.% film), and dwell times of 20 ms (1000 ppm film) and 25 ms (1 at.% film), which were enabled by on-the-fly data collection mode.[70] No chemical or structural changes to the films from the beam were observed.

ASSOCIATED CONTENT

ⓢ Supporting Information

The Supporting Information is available free of charge on the ACS Publications website at DOI: 10.1021/acsnano.7b02734.

> Details of solar cell device synthesis; additional J–V sweeps after prebias; solar cell boxplot summary for forward sweeps; helium-ion microscopy images of film morphology; X-ray diffraction data; additional XPS spectra of primary elements in MAPbI$_3$; alternate device structure device synthesis details and J–V results; absorptance data (PDF)

AUTHOR INFORMATION

Corresponding Authors
*E-mail: jpoindex@alum.mit.edu.
*E-mail: buonassisi@mit.edu.

ORCID Ⓘ
Jeremy R. Poindexter: 0000-0002-6616-9867
Robert L. Z. Hoye: 0000-0002-7675-0065
Lea Nienhaus: 0000-0003-1412-412X
Juan-Pablo Correa-Baena: 0000-0002-3860-1149
Moungi G. Bawendi: 0000-0003-2220-4365

Present Address
⊥Cavendish Laboratory, University of Cambridge, JJ Thomson Avenue, Cambridge CB3 0HE, UK.

Notes
The authors declare no competing financial interest.

REFERENCES

(1) Yang, W. S.; Noh, J. H.; Jeon, N. J.; Kim, Y. C.; Ryu, S.; Seo, J.; Seok, S. I. High-Performance Photovoltaic Perovskite Layers Fabricated through Intramolecular Exchange. *Science* **2015**, *348*, 1234–1237.

(2) Saliba, M.; Matsui, T.; Seo, J.-Y.; Domanski, K.; Correa-Baena, J.-P.; Nazeeruddin, M. K.; Zakeeruddin, S. M.; Tress, W.; Abate, A.; Hagfeldt, A.; Grätzel, M. Cesium-Containing Triple Cation Perovskite Solar Cells: Improved Stability, Reproducibility and High Efficiency. *Energy Environ. Sci.* **2016**, *9*, 1989–1997.

(3) Li, X.; Bi, D.; Yi, C.; Decoppet, J.-D.; Luo, J.; Zakeeruddin, S. M.; Hagfeldt, A.; Gratzel, M. A Vacuum Flash-Assisted Solution Process for High-Efficiency Large-Area Perovskite Solar Cells. *Science* **2016**, *353*, 58–62.

(4) Needleman, D. B.; Poindexter, J. R.; Kurchin, R. C.; Marius Peters, I.; Wilson, G.; Buonassisi, T. Economically Sustainable Scaling

of Photovoltaics to Meet Climate Targets. *Energy Environ. Sci.* **2016**, *9*, 2122−2129.

(5) Kojima, A.; Teshima, K.; Shirai, Y.; Miyasaka, T. Organometal Halide Perovskites as Visible-Light Sensitizers for Photovoltaic Cells. *J. Am. Chem. Soc.* **2009**, *131*, 6050−6051.

(6) Lee, M. M.; Teuscher, J.; Miyasaka, T.; Murakami, T. N.; Snaith, H. J. Efficient Hybrid Solar Cells Based on Meso-Superstructured Organometal Halide Perovskites. *Science* **2012**, *338*, 643−647.

(7) Kim, H.-S.; Lee, C.-R.; Im, J.-H.; Lee, K.-B.; Moehl, T.; Marchioro, A.; Moon, S.-J.; Humphry-Baker, R.; Yum, J.-H.; Moser, J. E.; Graetzel, M.; Park, N.-G. Lead Iodide Perovskite Sensitized All-Solid-State Submicron Thin Film Mesoscopic Solar Cell with Efficiency Exceeding 9%. *Sci. Rep.* **2012**, *2*, 583−585.

(8) Stranks, S. D.; Eperon, G. E.; Grancini, G.; Menelaou, C.; Alcocer, M. J. P.; Leijtens, T.; Herz, L. M.; Petrozza, A.; Snaith, H. J. Electron-Hole Diffusion Lengths Exceeding 1 Micrometer in an Organometal Trihalide Perovskite Absorber. *Science* **2013**, *342*, 341−344.

(9) deQuilettes, D. W.; Vorpahl, S. M.; Stranks, S. D.; Nagaoka, H.; Eperon, G. E.; Ziffer, M. E.; Snaith, H. J.; Ginger, D. S. Impact of Microstructure on Local Carrier Lifetime in Perovskite Solar Cells. *Science* **2015**, *348*, 683−686.

(10) Hutter, E. M.; Eperon, G. E.; Stranks, S. D.; Savenije, T. J. Charge Carriers in Planar and Meso-Structured Organic−Inorganic Perovskites: Mobilities, Lifetimes, and Concentrations of Trap States. *J. Phys. Chem. Lett.* **2015**, *6*, 3082−3090.

(11) Zakutayev, A.; Caskey, C. M.; Fioretti, A. N.; Ginley, D. S.; Vidal, J.; Stevanovic, V.; Tea, E.; Lany, S. Defect Tolerant Semiconductors for Solar Energy Conversion. *J. Phys. Chem. Lett.* **2014**, *5*, 1117−1125.

(12) Brandt, R. E.; Stevanović, V.; Ginley, D. S.; Buonassisi, T. Identifying Defect-Tolerant Semiconductors with High Minority-Carrier Lifetimes: Beyond Hybrid Lead Halide Perovskites. *MRS Commun.* **2015**, *5*, 265−275.

(13) Yin, W.-J.; Shi, T.; Yan, Y. Unusual Defect Physics in $CH_3NH_3PbI_3$ Perovskite Solar Cell Absorber. *Appl. Phys. Lett.* **2014**, *104*, 063903.

(14) Ledebo, L.-A.; Ridley, B. K. On the Position of Energy Levels Related to Transition-Metal Impurities in III-V Semiconductors. *J. Phys. C: Solid State Phys.* **1982**, *15*, L961−L964.

(15) Kleverman, M.; Omling, P.; Ledebo, L.-A.; Grimmeiss, H. G. Electrical Properties of Fe in GaAs. *J. Appl. Phys.* **1983**, *54*, 814.

(16) Caldas, M. J.; Fazzio, A.; Zunger, A. A Universal Trend in the Binding Energies of Deep Impurities in Semiconductors. *Appl. Phys. Lett.* **1984**, *45*, 671.

(17) Tersoff, J.; Harrison, W. A. Transition-Metal Impurities in Semiconductors—Their Connection with Band Lineups and Schottky Barriers. *Phys. Rev. Lett.* **1987**, *58*, 2367−2370.

(18) Srocka, B.; Scheffler, H.; Bimberg, D. Fe^{2+}-Fe^{3+} Level as a Recombination Center in $In_{0.53}Ga_{0.47}As$. *Phys. Rev. B: Condens. Matter Mater. Phys.* **1994**, *49*, 10259−10268.

(19) Su, J.; Chen, D. P.; Lin, C. T. Growth of Large $CH_3NH_3PbX_3$ (X = I, Br) Single Crystals in Solution. *J. Cryst. Growth* **2015**, *422*, 75−79.

(20) Chang, J.; Zhu, H.; Li, B.; Isikgor, F.; Hao, Y.; Xu, Q.; Ouyang, J. Boosting the Performance of Planar Heterojunction Perovskite Solar Cell by Controlling the Precursor Purity of Perovskite Materials. *J. Mater. Chem. A* **2016**, *4*, 887−893.

(21) Navas, J.; Sánchez-Coronilla, A.; Gallardo, J. J.; Cruz Hernández, N.; Piñero, J. C.; Alcántara, R.; Fernández-Lorenzo, C.; De los Santos, D. M.; Aguilar, T.; Martín-Calleja, J.; et al. New Insights into Organic−inorganic Hybrid Perovskite $CH_3NH_3PbI_3$ Nanoparticles. An Experimental and Theoretical Study of Doping in Pb^{2+} Sites with Sn^{2+}, Sr^{2+}, Cd^{2+} and Ca^{2+}. *Nanoscale* **2015**, *7*, 6216−6229.

(22) Abdelhady, A. L.; Saidaminov, M. I.; Murali, B.; Adinolfi, V.; Voznyy, O.; Katsiev, K.; Alarousu, E.; Comin, R.; Dursun, I.; Sinatra, L.; Sargent, E. H.; Mohammed, O. F.; Bakr, O. M. Heterovalent Dopant Incorporation for Bandgap and Type Engineering of Perovskite Crystals. *J. Phys. Chem. Lett.* **2016**, *7*, 295−301.

(23) Wang, J. T.-W.; Wang, Z.; Pathak, S.; Zhang, W.; DeQuilettes, D. W.; Wisnivesky-Rocca-Rivarola, F.; Huang, J.; Nayak, P. K.; Patel, J. B.; Mohd Yusof, H. A.; Vaynzof, Y.; Zhu, R.; Ramirez, I.; Zhang, J.; Ducati, C.; Grovenor, C.; Johnston, M. B.; Ginger, D. S.; Nicholas, R. J.; Snaith, H. J. Efficient Perovskite Solar Cells by Metal Ion Doping. *Energy Environ. Sci.* **2016**, *9*, 2892−2901.

(24) Pérez-del-Rey, D.; Forgács, D.; Hutter, E. M.; Savenije, T. J.; Nordlund, D.; Schulz, P.; Berry, J. J.; Sessolo, M.; Bolink, H. J. Strontium Insertion in Methylammonium Lead Iodide: Long Charge Carrier Lifetime and High Fill-Factor Solar Cells. *Adv. Mater.* **2016**, *28*, 9839−9845.

(25) Dunlap-Shohl, W. A.; Younts, R.; Gautam, B.; Gundogdu, K.; Mitzi, D. B. Effects of Cd Diffusion and Doping in High-Performance Perovskite Solar Cells Using CdS as Electron Transport Layer. *J. Phys. Chem. C* **2016**, *120*, 16437−16445.

(26) Shi, T.; Yin, W.-J.; Yan, Y. Predictions for P-Type $CH_3NH_3PbI_3$ Perovskites. *J. Phys. Chem. C* **2014**, *118*, 25350−25354.

(27) Klug, M. T.; Osherov, A.; Haghighirad, A. A.; Stranks, S. D.; Brown, P. R.; Bai, S.; Wang, J. T.-W.; Dang, X.; Bulović, V.; Snaith, H. J.; Belcher, A. M. Tailoring Metal Halide Perovskites through Metal Substitution: Influence on Photovoltaic and Material Properties. *Energy Environ. Sci.* **2017**, *10*, 236−246.

(28) Istratov, A. A.; Hieslmair, H.; Weber, E. R. Iron Contamination in Silicon Technology. *Appl. Phys. A: Mater. Sci. Process.* **2000**, *70*, 489−534.

(29) Henley, W. B.; Ramappa, D. A. Iron Precipitation in Float Zone Grown Silicon. *J. Appl. Phys.* **1997**, *82*, 589.

(30) Davis, J. R.; Rohatgi, A.; Hopkins, R. H.; Blais, P. D.; Rai-Choudhury, P.; McCormick, J. R.; Mollenkopf, H. C. Impurities in Silicon Solar Cells. *IEEE Trans. Electron Devices* **1980**, *27*, 677−687.

(31) Istratov, A. A.; Hieslmair, H.; Weber, E. R. Iron and Its Complexes in Silicon. *Appl. Phys. A: Mater. Sci. Process.* **1999**, *69*, 13−44.

(32) van Kooten, J. J.; Sieverts, E. G.; Ammerlaan, C. A. J. Electron-Nuclear Double Resonance of Interstitial Positively Charged Iron in Silicon. *Phys. Rev. B: Condens. Matter Mater. Phys.* **1988**, *37*, 8949−8957.

(33) Collord, A. D.; Xin, H.; Hillhouse, H. W. Combinatorial Exploration of the Effects of Intrinsic and Extrinsic Defects in $Cu_2ZnSn(S,Se)_4$. *IEEE J. Photovolt.* **2015**, *5*, 288−298.

(34) Schmidt, J.; Lim, B.; Walter, D.; Bothe, K.; Gatz, S.; Dullweber, T.; Altermatt, P. P. Impurity-Related Limitations of Next-Generation Industrial Silicon Solar Cells. *IEEE J. Photovolt.* **2013**, *3*, 114−118.

(35) Stoumpos, C. C.; Malliakas, C. D.; Kanatzidis, M. G. Semiconducting Tin and Lead Iodide Perovskites with Organic Cations: Phase Transitions, High Mobilities, and Near-Infrared Photoluminescent Properties. *Inorg. Chem.* **2013**, *52*, 9019−9038.

(36) Alkauskas, A.; McCluskey, M. D.; Van de Walle, C. G. Tutorial: Defects in semiconductors—Combining Experiment and Theory. *J. Appl. Phys.* **2016**, *119*, 181101.

(37) Biesinger, M. C.; Payne, B. P.; Grosvenor, A. P.; Lau, L. W. M.; Gerson, A. R.; Smart, R. S. C. Resolving Surface Chemical States in XPS Analysis of First Row Transition Metals, Oxides and Hydroxides: Cr, Mn, Fe, Co and Ni. *Appl. Surf. Sci.* **2011**, *257*, 2717−2730.

(38) Grosvenor, A. P.; Kobe, B. A.; Biesinger, M. C.; McIntyre, N. S. Investigation of Multiplet Splitting of Fe 2p XPS Spectra and Bonding in Iron Compounds. *Surf. Interface Anal.* **2004**, *36*, 1564−1574.

(39) Morishige, A. E.; Laine, H. S.; Schön, J.; Haarahiltunen, A.; Hofstetter, J.; del Cañizo, C.; Schubert, M. C.; Savin, H.; Buonassisi, T. Building Intuition of Iron Evolution during Solar Cell Processing through Analysis of Different Process Models. *Appl. Phys. A: Mater. Sci. Process.* **2015**, *120*, 1357−1373.

(40) Hofstetter, J.; Fenning, D. P.; Powell, D. M.; Morishige, A. E.; Wagner, H.; Buonassisi, T. Sorting Metrics for Customized Phosphorus Diffusion Gettering. *IEEE J. Photovolt.* **2014**, *4*, 1421−1428.

(41) Zoth, G.; Bergholz, W. A Fast, Preparation-free Method to Detect Iron in Silicon. *J. Appl. Phys.* **1990**, *67*, 6764−6771.

(42) Graff, K.; Pieper, H. The Behavior of Transition and Noble Metals in Silicon Crystals. In *Semiconductor Silicon 1981*; Huff, H. R., Kriegler, R. J., Takeishi, Y., Eds.; Electrochemical Society: Pennington, NJ, 1981; p 331.

(43) Shockley, W.; Read, W. Statistics of the Recombinations of Holes and Electrons. *Phys. Rev.* **1952**, *87*, 835−842.

(44) Hall, R. Electron-Hole Recombination in Germanium. *Phys. Rev.* **1952**, *87*, 387−387.

(45) Correa Baena, J. P.; Steier, L.; Tress, W.; Saliba, M.; Neutzner, S.; Matsui, T.; Giordano, F.; Jacobsson, T. J.; Srimath Kandada, A. R.; Zakeeruddin, S. M.; Petrozza, A.; Abate, A.; Nazeeruddin, M. K.; Grätzel, M.; Hagfeldt, A. Highly Efficient Planar Perovskite Solar Cells through Band Alignment Engineering. *Energy Environ. Sci.* **2015**, *8*, 2928−2934.

(46) Buonassisi, T.; Istratov, A. A.; Pickett, M. D.; Marcus, M. A.; Hahn, G.; Riepe, S.; Isenberg, J.; Warta, W.; Willeke, G.; Ciszek, T. F.; Weber, E. R. Quantifying the Effect of Metal-Rich Precipitates on Minority Carrier Diffusion Length in Multicrystalline Silicon Using Synchrotron-Based Spectrally Resolved X-Ray Beam-Induced Current. *Appl. Phys. Lett.* **2005**, *87*, 044101.

(47) Plekhanov, P. S.; Gafiteanu, R.; Gösele, U. M.; Tan, T. Y. Modeling of Gettering of Precipitated Impurities from Si for Carrier Lifetime Improvement in Solar Cell Applications. *J. Appl. Phys.* **1999**, *86*, 2453−2458.

(48) Kwapil, W.; Schon, J.; Schindler, F.; Warta, W.; Schubert, M. C. Impact of Iron Precipitates on Carrier Lifetime in As-Grown and Phosphorus-Gettered Multicrystalline Silicon Wafers in Model and Experiment. *IEEE J. Photovolt.* **2014**, *4*, 791−798.

(49) Onoda-Yamamuro, N.; Matsuo, T.; Suga, H. Dielectric Study of $CH_3NH_3PbX_3$ (X = Cl, Br, I). *J. Phys. Chem. Solids* **1992**, *53*, 935−939.

(50) Lin, Q.; Armin, A.; Nagiri, R. C. R.; Burn, P. L.; Meredith, P. Electro-Optics of Perovskite Solar Cells. *Nat. Photonics* **2014**, *9*, 106−112.

(51) Eames, C.; Frost, J. M.; Barnes, P. R. F.; O'Regan, B. C.; Walsh, A.; Islam, M. S. Ionic Transport in Hybrid Lead Iodide Perovskite Solar Cells. *Nat. Commun.* **2015**, *6*, 7497.

(52) Correa-Baena, J.-P.; Turren-Cruz, S.-H.; Tress, W.; Hagfeldt, A.; Aranda, C.; Shooshtari, L.; Bisquert, J.; Guerrero, A. Changes from Bulk to Surface Recombination Mechanisms between Pristine and Cycled Perovskite Solar Cells. *ACS Energy Lett.* **2017**, *2*, 681−688.

(53) van Reenen, S.; Kemerink, M.; Snaith, H. J. Modeling Anomalous Hysteresis in Perovskite Solar Cells. *J. Phys. Chem. Lett.* **2015**, *6*, 3808−3814.

(54) Docampo, P.; Ball, J. M.; Darwich, M.; Eperon, G. E.; Snaith, H. J. Efficient Organometal Trihalide Perovskite Planar-Heterojunction Solar Cells on Flexible Polymer Substrates. *Nat. Commun.* **2013**, *4*, 2761.

(55) Powell, D. M.; Fu, R.; Horowitz, K.; Basore, P. A.; Woodhouse, M.; Buonassisi, T. The Capital Intensity of Photovoltaics Manufacturing: Barrier to Scale and Opportunity for Innovation. *Energy Environ. Sci.* **2015**, *8*, 3395−3408.

(56) Noel, N. K.; Stranks, S. D.; Abate, A.; Wehrenfennig, C.; Guarnera, S.; Haghighirad, A.-A.; Sadhanala, A.; Eperon, G. E.; Pathak, S. K.; Johnston, M. B.; Petrozza, A.; Herz, L. M.; Snaith, H. J. Lead-Free Organic-Inorganic Tin Halide Perovskites for Photovoltaic Applications. *Energy Environ. Sci.* **2014**, *7*, 3061.

(57) Hao, F.; Stoumpos, C. C.; Cao, D. H.; Chang, R. P. H.; Kanatzidis, M. G. Lead-Free Solid-State Organic−inorganic Halide Perovskite Solar Cells. *Nat. Photonics* **2014**, *8*, 489−494.

(58) Sun, Y.-Y.; Shi, J.; Lian, J.; Gao, W.; Agiorgousis, M. L.; Zhang, P.; Zhang, S. Discovering Lead-Free Perovskite Solar Materials with a Split-Anion Approach. *Nanoscale* **2016**, *8*, 6284−6289.

(59) Ganose, A. M.; Savory, C. N.; Scanlon, D. O. Beyond Methylammonium Lead Iodide: Prospects for the Emergent Field of ns^2 Containing Solar Absorbers. *Chem. Commun.* **2017**, *53*, 20−44.

(60) Hoye, R. L. Z.; Brandt, R. E.; Osherov, A.; Stevanović, V.; Stranks, S. D.; Wilson, M. W. B.; Kim, H.; Akey, A. J.; Perkins, J. D.; Kurchin, R. C.; Poindexter, J. R.; Wang, E. N.; Bawendi, M. G.; Bulović, V.; Buonassisi, T. Methylammonium Bismuth Iodide as a Lead-Free, Stable Hybrid Organic-Inorganic Solar Absorber. *Chem. - Eur. J.* **2016**, *22*, 2605−2610.

(61) Rahayu, S. U.; Chou, C.-L.; Suriyawong, N.; Aragaw, B. A.; Shi, J.-B.; Lee, M.-W. Sodium Antimony Sulfide ($NaSbS_2$): Turning an Unexpected Impurity into a Promising, Environmentally Friendly Novel Solar Absorber Material. *APL Mater.* **2016**, *4*, 116103.

(62) Kresse, G.; Furthmüller, J. Efficient Iterative Schemes for *Ab Initio* Total-Energy Calculations Using a Plane-Wave Basis Set. *Phys. Rev. B: Condens. Matter Mater. Phys.* **1996**, *54*, 11169−11186.

(63) Perdew, J. P.; Burke, K.; Ernzerhof, M. Generalized Gradient Approximation Made Simple. *Phys. Rev. Lett.* **1996**, *77*, 3865−3868.

(64) Lany, S.; Zunger, A. Assessment of Correction Methods for the Band-Gap Problem and for Finite-Size Effects in Supercell Defect Calculations: Case Studies for ZnO and GaAs. *Phys. Rev. B: Condens. Matter Mater. Phys.* **2008**, *78*, 235104.

(65) Peng, H.; Scanlon, D. O.; Stevanovic, V.; Vidal, J.; Watson, G. W.; Lany, S. Convergence of Density and Hybrid Functional Defect Calculations for Compound Semiconductors. *Phys. Rev. B: Condens. Matter Mater. Phys.* **2013**, *88*, 115201.

(66) Goyal, A.; Gorai, P.; Peng, H.; Lany, S.; Stevanović, V. A Computational Framework for Automation of Point Defect Calculations. *Comput. Mater. Sci.* **2017**, *130*, 1−9.

(67) Monkhorst, H. J.; Pack, J. D. Special Points for Brillouin-Zone Integrations. *Phys. Rev. B* **1976**, *13*, 5188−5192.

(68) Stevanović, V.; Lany, S.; Zhang, X.; Zunger, A. Correcting Density Functional Theory for Accurate Predictions of Compound Enthalpies of Formation: Fitted Elemental-Phase Reference Energies. *Phys. Rev. B: Condens. Matter Mater. Phys.* **2012**, *85*, 115104.

(69) Cai, Z.; Lai, B.; Yun, W.; McNulty, I.; Khounsary, A.; Maser, J.; Ilinsky, P.; Legnini, D.; Trakhtenberg, E.; Xu, S.; Tieman, B.; Wiemerslage, G.; Gluskin, E. Performance of a High-Resolution X-ray Microprobe at the Advanced Photon Source. In *AIP Conference Proceedings*; AIP, 2000; Vol. *521*, pp 31−34.

(70) Morishige, A. E.; Laine, H. S.; Looney, E. E.; Jensen, M. A.; Vogt, S.; Li, J. B.; Lai, B.; Savin, H.; Buonassisi, T. Increased Throughput and Sensitivity of Synchrotron-Based Characterization for Photovoltaic Materials. *IEEE J. Photovolt.* **2017**, *7*, 763−771.